

Nonlinear behaviors of a comb drive actuator under electrically induced tensile and compressive stresses

Ki Bang Lee¹, Albert P Pisano² and Liwei Lin²

¹ KB Lab, 46B Toh Tuck Road #04-12, Singapore 596748

² Berkeley Sensor and Actuator Center, Department of Mechanical Engineering, University of California at Berkeley, USA

E-mail: kblee@kblab.biz and kibanglee@hotmail.com

Received 10 October 2006, in final form 16 January 2007

Published 14 February 2007

Online at stacks.iop.org/JMM/17/557

Abstract

A theory with experimental verifications has been developed to investigate the nonlinear behavior of comb drive actuators under applied external electrical potential and Joule heating effects. The nonlinear behavior originates from coupled effects of the beam structure under applied electrical potential with electrostatically induced tensile stress and thermally induced compressive stress. Detailed analyses have been conducted to study the nonlinear spring force, residual and thermal stresses, as well as the dynamic behaviors of the actuator. Experimental and numerical simulation results based on an energy model have been proposed to analyze the linear and cubic stiffness as well as frequency changes of the comb drive actuators. Theories and models developed on the comb drive actuator in this work could be extended to explain nonlinearity and dynamic behaviors of more complicated microsystems encountering other force-induced nonlinear sources.

(Some figures in this article are in colour only in the electronic version)

1. Introduction

The invention of the comb drive actuator [1] inspired the development of many sensors and actuators [2–6], as comb-shape actuators are easy to make and provide good linearity under small deflections. Most devices or systems based on comb drive actuators use the linear model to calculate the stiffness of the suspension spring. For instance, a linear spring model of folded spring design [1] has been assumed to describe the dynamic behaviors of comb drive actuators. However, transducers based on electrostatic resonators, such as microgyroscopes or microaccelerometers, may require post-fabrication frequency tuning to improve their sensitivity and performance and nonlinear behavior can be introduced. Various frequency tuning schemes have been demonstrated by actively introducing external electrical forces or permanently altering the geometry of the comb actuators. For example, the frequency of the microactuators has been tuned by applying a control voltage to triangular electrostatic comb arrays for about

3% reduction in frequency [7], by adding material deposition to the mass for about 1.2% reduction in frequency [8] or by thermally expanding microstructures for up to 25% reduction in frequency [9, 10]. Other frequency-tuning methods can cause frequency reduction due to externally applied attractive force [7], mass increase [8] or thermal expansion [9, 10] of the spring structure. Using electrostatic fringing-field actuators [11], researchers have tuned the effective linear and cubic stiffness of microstructures. However this electrostatic tuning method generally requires high tuning voltages of up to 35 V. In these and other situations where external forces/mechanisms are used to modify the performances of comb-shape actuators, nonlinear behavior could emerge and should be modeled and formulated. This paper presents a theory with experimental demonstrations to illustrate nonlinear behaviors of the comb-shape actuators under externally induced forces, including externally applied electrical potential and Joule heating effects.

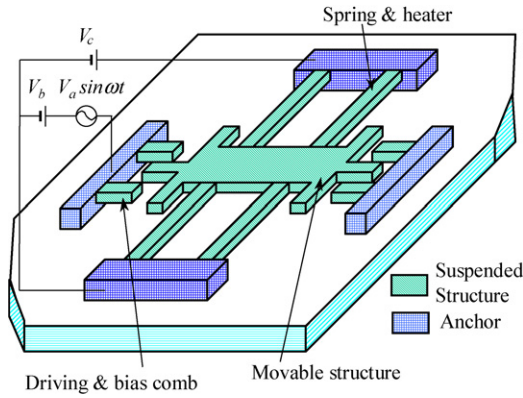


Figure 1. Comb drive actuator using tension and compression effects of springs (beams): the dc bias voltage V_b is used to provide the tension in the spring beam, while the control voltage, V_c , causes the compression of the spring by Joule heating.

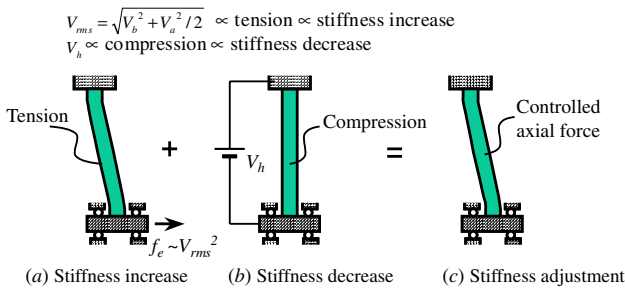


Figure 2. Basic concept showing stiffness increase and decrease: (a) the root mean square voltage, V_{rms} , of the comb drive generates tension in a beam to increase its stiffness, (b) the heating voltage V_h causes thermal expansion and compressive stress to reduce the stiffness. A combination of these provides a unique way to either increase or decrease the stiffness of a mechanical structure.

2. Theory

Figure 1 shows a schematic of the comb drive microactuator utilizing tension and compression effects of springs to alter its resonant frequency. The movable structure suspended by the spring beams is actuated in the lateral direction by applying a dc bias voltage V_b and ac driving voltage V_a . The dc bias voltage V_b and a Joule heating voltage V_c are used to tune the linear and cubic stiffness of the spring to generate tension or compression effects.

Figure 2 shows the principle of stiffness change of the spring beam when dc bias voltage V_b and the heating voltage V_h are applied. The dc bias voltage V_b generates electrostatic tensile force to cause deflection of the beam as illustrated in figure 2(a). The heating voltage causes the beam to extend as the beam stiffness decreases due to compressive force as illustrated in figure 2(b). In the following analyses, the nonlinear stiffness behavior of the spring beam is first described and the dynamic behavior of the comb resonators is afterward derived.

2.1. Behavior of the springs

A straight beam in figure 3(a) with Young's modulus E , moment of inertia I , length l , width b and the initial tension

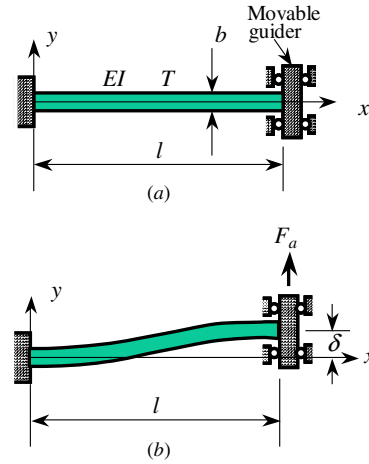


Figure 3. Deflection of a beam subjected to an applied force. (a) Configuration before applying a force, (b) beam subjected to an applied force.

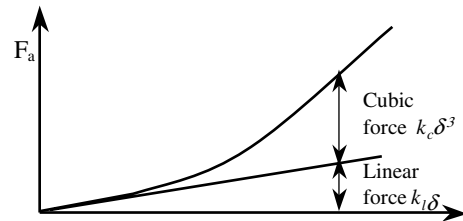


Figure 4. Force with respect to deflection of the spring beam. The force is the sum of the linear and cubic forces.

T is subjected to an applied force F_a in the upward direction with deflection, δ , as illustrated in figure 3(b). Figure 4 depicts the force that was generated by the beam when the beam is deflected by δ . The force, F_a , can be modeled as the sum of the linear force term and the cubic force term due to the geometric nonlinearity, the initial stress and other effects. Because the beam is symmetric about the axis x in figure 3, the quadratic and forth forces disappear and the linear and cubic forces are included in the spring force formulation. In order to obtain the force under a given deflection, we combine theoretical solution for the linear force and numerical solution for the cubic force term and assume the following relationship: $F_a = k_l \delta + k_c \delta^3$.

We use the dimensional analysis [14] to obtain a simple force–deflection equation from the nonlinear curves of figure 4 as follows:

$$f_1(F_a, \delta, EI, l, b, T) = 0. \quad (1)$$

Four dimensionless parameters that govern the beam deflection can be obtained as follows [14]:

$$\frac{l^2 F_a}{EI} = f_2\left(\frac{\delta}{l}, \frac{l^2 T}{EI}, \frac{b}{l}\right) \quad (2)$$

where $\frac{l^2 F_a}{EI}$, $\frac{\delta}{l}$, $\frac{l^2 T}{EI}$ and $\frac{b}{l}$ are the dimensionless parameters. By assuming that the tension T in the beam is constant and that the beam deflection is small, we can obtain the linear force F_a at the deflection δ as [13]:

$$F_a = k_l \delta \quad (3)$$

where

$$\frac{k_1}{k} = \frac{1}{12} \frac{\lambda^3 \sinh \lambda}{\lambda \sinh \lambda + 2(1 - \cosh \lambda)} \quad (4)$$

$$k = \frac{12EI}{l^3} \quad (5)$$

$$\lambda = l \sqrt{\frac{T}{EI}}. \quad (6)$$

If a compressive force P instead of the tension T is applied in equation (4), the buckling load P of the spring beam can be obtained as $P = \pi^2 EI / l^2$ from $k_1 = 0$ or $\sinh(l\sqrt{-P/EI}) = i \sin(l\sqrt{P/EI}) = 0$. After using Taylor's series expansion to equation (4), a simple linear stiffness is obtained for small λ :

$$\begin{aligned} \frac{k_1}{k} &= 1 + \frac{1}{10} \lambda^2 - \frac{1}{8400} \lambda^4 + \text{high order terms} \\ &\cong 1 + \frac{1}{10} \lambda^2 = 1 + \frac{1}{10} \frac{l^2 T}{EI}. \end{aligned} \quad (7)$$

It is noted in equation (7) that the linear stiffness is proportional to the initial tension T when $l^2 T / EI$ is small. The linear stiffness k_1 represents the linear force while the cubic force can be obtained from a numerical simulation. After combining the linear force of equation (3) with the cubic force, the applied force at the deflection δ can be obtained as follows:

$$F_a = k_1 \delta + k_c \delta^3 \quad (8)$$

where

$$k_1 = k_{10} + k_{11} \sigma_i \quad (9)$$

$$k_{10} = k = \frac{12EI}{l^3} \quad (10)$$

$$k_{11} = k \frac{1}{10} \frac{l^2 A}{EI} = \frac{6}{5} \frac{A}{l} \quad (11)$$

$$\sigma_i = \frac{T}{A}. \quad (12)$$

σ_i is the initial stress that consists of the residual stress and the thermal stress that may be generated by the Joule heating. Subtracting the linear force of the equation (8) from the spring beam force of figure 4 and using a curve fitting technique gives the cubic stiffness reflecting the cubic force,

$$k_c = k_{c0} + k_{c1} \sigma_i + k_{c2} \sigma_i^2 \quad (13)$$

where k_{c0} , k_{c1} and k_{c2} denote coefficients to determine the cubic stiffness k_c at a given initial stress σ_i . A procedure to obtaining the coefficients for the cubic stiffness will be detailed in section 3.

2.2. Compressive stress generation in the spring

The spring beam of figure 1 also acts as a heater for adjusting thermal stress. Figure 5 shows the energy balance of an infinitesimal beam element taken from the spring beam. In order to analyze temperature distribution of the beam, the one-dimensional energy balance equation is used [21]:

$$\begin{aligned} \dot{Q} dx - k_{th} A \frac{\partial \theta}{\partial x} &= hp dx (\theta - \theta_\infty) \\ -k_{th} A \frac{\partial \theta}{\partial x} + \frac{\partial}{\partial x} \left(-k_{th} A \frac{\partial \theta}{\partial x} \right) dx & \end{aligned} \quad (14)$$

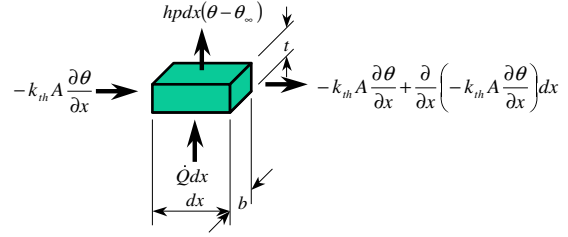


Figure 5. Energy balance of an infinitesimal beam element.

where

$$\dot{Q} = \frac{V_h^2}{RI}. \quad (15)$$

Equation (14) is rewritten as follows:

$$k_{th} A \frac{d^2 \theta}{dx^2} - hp (\theta - \theta_\infty) + \dot{Q} = 0. \quad (16)$$

Before solving the above equation, we examine the second term reflecting the convection heat transfer. With a characteristic temperature θ_{max} and the characteristic length l , a dimensionless number Ψ_1 can be defined to compare the conduction heat transfer (the first term of equation (16)) with convection heat transfer (the second term of equation (16)):

$$\Psi_1 = \frac{[hp(\theta - \theta_\infty)]}{[k_{th} A \frac{d^2 \theta}{dx^2}]} = \frac{hp \theta_{max}}{k_{th} A \frac{\theta_{max}}{l^2}} = \frac{hpl^2}{k_{th} A}. \quad (17)$$

The dimensionless parameter Ψ_1 is calculated as 0.0063 when we use dimensions and values of typical silicon micromachined comb drive actuators: $l \sim 100 \times 10^{-6}$ m, $p \sim 10 \times 10^{-6}$ m, $h \sim 5$ W m⁻² °C⁻¹, $k_{th} \sim 20$ W m⁻¹ °C⁻¹, $A \sim 4 \times 10^{-12}$ m². $\Psi_1 \ll 1$ implies that the convection heat transfer is very small compared to the heat conduction transfer, so that the convection heat transfer could be ignored. Dropping the second term of equation (16), we rewrite the differential equation as follows:

$$\frac{d^2 \theta}{dx^2} + \frac{\dot{Q}}{k_{th} A} = 0. \quad (18)$$

With the boundary conditions $\theta = \theta_\infty$ at $x = 0$ and $x = l$, the above equation yields the temperature distribution equation [21]

$$\theta - \theta_\infty = \frac{\dot{Q}}{2k_{th} A} \left(\frac{l^2}{2} - \left(x - \frac{l}{2} \right)^2 \right). \quad (19)$$

The temperature distribution is quadratic and the maximum temperature $(\theta - \theta_\infty)_{max}$ is $\frac{\dot{Q} l^2}{4k_{th} A}$ at $x = l/2$. One can obtain the thermally induced strain from the integration of equation (19) on x :

$$\frac{\Delta l}{l} = \frac{1}{l} \alpha \int_0^l \frac{\dot{Q}}{2k_{th} A} \left(\frac{l^2}{2} - \left(x - \frac{l}{2} \right)^2 \right) dx = \frac{\alpha \dot{Q} l^2}{12k_{th} A}. \quad (20)$$

Using the above strain, the initial tension and stress are expressed as follows:

$$T = \sigma_r A - EA \frac{\Delta l}{l} = \sigma_r A - \frac{E \alpha \dot{Q} l^2}{12k_{th}} \quad (21)$$

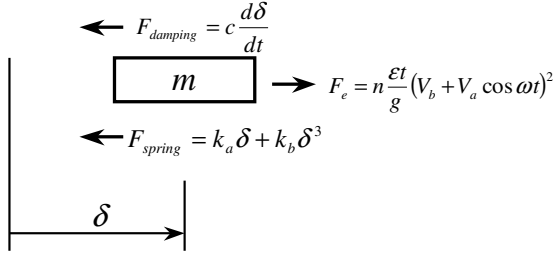


Figure 6. Forces acting on the movable structure.

$$\sigma_i = \frac{T}{A} = \sigma_r - \frac{E\alpha \dot{Q}l^2}{12k_{th}A} \quad (22)$$

where σ_r is the residual stress at $\dot{Q} = 0$. It is noted from equations (15), (21) and (22) that the initial tension and stress decreases with increasing heating voltage. When the tension T due to the heating reaches the buckling load of zero linear stiffness (equation (4)), the beam is buckled. The vibration of microactuators with buckled beam can extend travel range as shown in the following sections.

2.3. Dynamic behaviors of the movable structure

Figure 6 shows the forces on the movable structures when it moves to the right-hand side. The electrostatic force F_e of the comb is a driving force, damping force $F_{damping}$ is a drag force and spring force F_{spring} is a restoring force. The equation of motion is obtained from Newton's law,

$$m \frac{d^2\delta}{dt^2} + c \frac{d\delta}{dt} + k\delta = F_e \quad (23)$$

where

$$k = k_a + k_b\delta^2 \quad (24)$$

$$k_a = N_s k_l \quad (25)$$

$$k_b = N_s k_c \quad (26)$$

$$F_e = n \frac{\epsilon t_s}{g} (V_b + V_a \cos \omega t)^2 \quad (27)$$

$$c = c_p \beta h_s \left(1 + \frac{\sinh 2\beta h_s + \sin 2\beta h_s}{\cosh 2\beta h_s - \cos 2\beta h_s} + \frac{A_f}{A_p} \frac{\sinh 2\beta g + \sin 2\beta g}{\cosh 2\beta g - \cos 2\beta g} \right) \quad (28)$$

$$c_p = \frac{\mu A_p}{h_s} \quad (29)$$

$$\beta = \left(\frac{\omega}{2\nu} \right)^{1/2} \quad (30)$$

c denotes the damping coefficient from the Stokes' damping model [15, 22] and c_p is the Couette damping coefficient [22] due to the Couette shear flow [23] between the movable structure and the substrate.

Equations (23)–(30) include severe nonlinearities such as the cubic stiffness, the initial stress effect, the bias voltage change, the geometric nonlinearity, the angular frequency and the damping coefficient as a function of the angular frequency, so that we cannot use simple equations and solutions such as the Duffing's equation [16, 17]. To solve the preceding

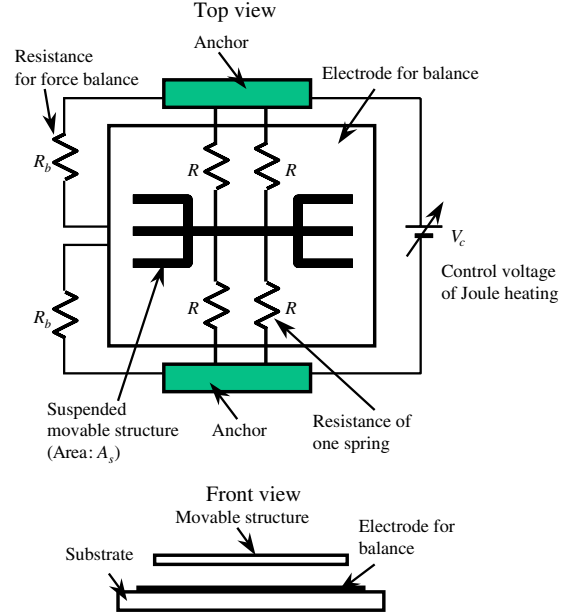


Figure 7. Electrical connection to heat the beams and to avoid the stiction of the movable structure to the substrate.

nonlinear equation of equation (23), the Park method [18] is used that is one of the stable methods for solving nonlinear second differential equations. Applying the Park method to the equation (23) gives the following equation:

$$\bar{m} \delta_{t+\Delta t} = \bar{F}_{e,t+\Delta t} \quad (31)$$

$$\bar{m} = \frac{100}{36\Delta t^2} m + \frac{10}{6\Delta t} c + k \quad (32)$$

$$\begin{aligned} \bar{F}_{e,t+\Delta t} = & F_{e,t+\Delta t} + \frac{15}{6\Delta t} m \dot{\delta}_t - \frac{1}{\Delta t} m \dot{\delta}_{t-\Delta t} + \frac{1}{6\Delta t} m \dot{\delta}_{t-2\Delta t} \\ & + \left(\frac{150}{36\Delta t^2} m + \frac{15}{6\Delta t} c \right) \delta_t - \left(\frac{10}{6\Delta t^2} m + \frac{1}{\Delta t} c \right) \delta_{t-\Delta t} \\ & + \left(\frac{10}{36\Delta t^2} m + \frac{1}{6\Delta t} c \right) \delta_{t-2\Delta t} \end{aligned} \quad (33)$$

where subscript t is time, subscript Δt is time step, $\dot{\delta}$ denotes the velocity ($d\delta/dt$). The Wilson theta method [18] is used to obtain the first two steps of displacement (δ) and velocity ($\dot{\delta}$) at $t - \Delta t$ and $t - 2\Delta t$. With the initial displacement and the velocity at $t = 0$ and the first two steps, the displacements of the next time steps are successively calculated.

3. Design and fabrication

When the Joule heating voltage is applied as shown in figure 1, the movable structure has electric potential that generates an electrostatic force in the direction normal to the substrate. This nonlinear electrostatic force pushes the movable structure downward and may result in the collapse of the movable structure into the substrate [27]. In order to avoid structure collapse, the voltage of the lower electrode is set equal to that of the movable structure. Figure 7 depicts the electrical wiring to heat the beams and to avoid the collapse of the lower electrode. In figure 7, the beam resistance is R and

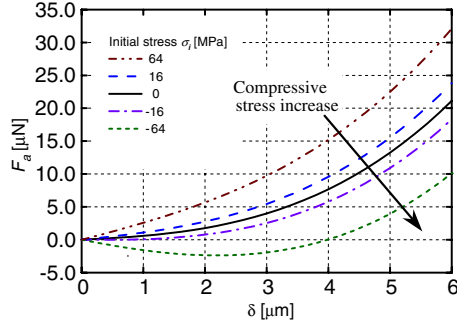


Figure 8. Force with respect to deflection. The nonlinear beam deflection is obtained from a simulation using commercial software, ABACUS, with $l = 150 \mu\text{m}$, $b = 2 \mu\text{m}$, t_s (thickness) $= 2 \mu\text{m}$ and $E = 110 \text{ GPa}$.

the resistance for force balance is R_b . The voltage V_h of the movable structure is obtained as

$$V_h = \frac{1/(\frac{1}{R} + \frac{1}{R})}{1/(\frac{1}{R} + \frac{1}{R}) + 1/(\frac{1}{R} + \frac{1}{R})} V_c = \frac{V_c}{2}. \quad (34)$$

Similarly, the voltage of the lower electrode for balance has the same voltage. It is noted that the voltage V_h of equation (34) is also used to generate Joule heating (equation (15)) in a beam to induce the thermal compressive stress. Table 2 summarizes the design parameters of the comb drive actuator that can adjust the linear and cubic stiffness as well as the resonant frequency.

The linear and cubic stiffness of the spring beam shown in table 3 is obtained by using the beam data in table 2 and ABACUS [19]—a finite element simulation software. The numerical simulation using ABACUS gives the force F_a at deflection δ as shown in figure 8. The force increases with deflection but decreases when compressive stress is increased (i.e. negative initial stress). When the initial compressive stress increases, the linear stiffness and the force in a portion of deflections become negative. For the initial stress of -64 MPa in figure 8, the force is negative in the range of $0-4 \mu\text{m}$ and the stiffness is negative in the range of $0-2.2 \mu\text{m}$. Subtracting the linear force ($k_l\delta$ of equation (8)) from the simulated force of figure 8 gives the cubic force that is a function of the initial stress, σ_i . From a polynomial curve fitting of the cubic force, the cubic stiffness coefficients of equation (13) are obtained. Table 3 summarizes the coefficients of the linear and cubic stiffness and table 4 shows the initial stress, the linear and cubic stiffness as functions of V_c . The cubic stiffness of table 2 is in agreement with that from figure 8 within 3% discrepancy in the range of $-64 \text{ MPa} \leq \sigma_i \leq 64 \text{ MPa}$. When the heating control voltage V_c increases from 0 to 2 V in table 4, the initial stress in each beam decreases from the residual stress.

Using the computational scheme of equation (31) and the design parameters in tables 2 and 3, we numerically simulate the nonlinear dynamics of the comb drive actuator under ac driving voltage $V_a = 10 \text{ V}$ with dc bias voltage $V_b = 40 \text{ V}$. Figures 9 and 10 show the four possible responses. In figure 9, the movable structure with zero heating voltage at time $t = 0$ is driven by the electrostatic force of the comb (equation (27)). Without heating, the displacement of the movable structure increases with time and the amplitude reaches a saturation level. When the heating voltage $V_c = 2 \text{ V}$ is applied to the beam, three possible modes are shown in figures 10(a), (b)

Table 1. List of parameters.

b	Beam width
c	Damping coefficient
c_p	Couette damping coefficient
f	Frequency
g	Gap between the movable and stationary fingers
h	Convection heat-transfer coefficient of the air
h_s	Gap between the movable structure and the substrate
k	Stiffness of a beam
k_a	Linear stiffness of the four spring beams
k_b	Cubic stiffness of the four spring beams
k_c	Cubic stiffness
k_{c0}, k_{c1} and k_{c2}	Coefficients of the cubic stiffness
k_{eff}	Effective stiffness
k_l	Linear stiffness
k_{l0} and k_{l1}	Coefficients of the linear stiffness
k_{th}	Conductivity of the beam
l	Beam length
m	Mass
n	Number of fingers of the movable structure for the electrostatic force
p	Perimeter defined as $2(b + t_s)$
t	Time
t_s	Structure thickness
x, y, z	Coordinates
A	Cross-sectional area of the beam
A_f	Area of fingers for the damping
A_p	Plate area
E	Potential energy or Young's modulus
E_b	Barrier energy
E_δ	Maximum energy stored in the beam
EI	Bending modulus of the beam
F_a	Applied force
F_e	Electrostatic force
N_s	Number of the spring beams
Q	Generated heat per unit beam length
R	Resistance of the beam
R_b	Resistance for force balance
T	Initial tension
V_a	ac driving voltage
V_c	Voltage across the beams
V_d	dc bias voltage
V_h	Heating voltage across the beam
α	Coefficient of thermal expansion
δ	Displacement
$\dot{\delta}$	Velocity ($d\delta/dt$)
ϵ	Permittivity of air
μ	Dynamic viscosity
ν	Kinematic viscosity
θ	Temperature
θ_∞	Atmospheric temperature
ρ	Density
σ_i	Initial stress
σ_r	Residual stress
ω	Angular frequency of the ac voltage
Δl	Thermal expansion of the beam length
Δt	Time step
Ψ_1	Dimensionless number to compare the conduction heat transfer with convection heat transfer

and (c). Under the resonant frequency of 16 kHz, the movable structure in figure 10(a) swings a few times in the positive and negative regions and thereafter its motion is confined in the positive region. The second case is observed in figure 10(b). When the driving voltage is applied at $f = 16.5 \text{ kHz}$, the movable structure vibrates a few times in the positive and negative regions and then its motion is confined in the negative region. At $f = 17 \text{ kHz}$, the movable structure continuously moves in both the directions even though its motion is confined

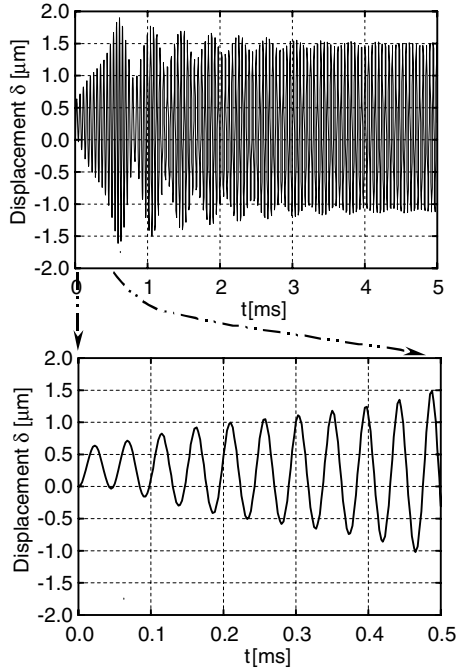


Figure 9. Simulated displacement with respect to time under the heating voltage $V_c = 0$ V and actuating frequency $f = 21.25$ kHz: an ac driving voltage of 10 V with dc bias voltage $V_b = 40$ V is applied to the comb in figure 1 to actuate the movable structure.

Table 2. Design parameters of a comb drive actuator.

Movable structure	
Mass of movable structure, m	6.36×10^{-11} kg
Area of movable structure, A_m	1.37×10^{-8} m ²
Gap between the movable structure and the substrate, h	2×10^{-6} m
Spring beam	
Number of spring beams, N_s	4
Thickness, t_s	2×10^{-6} m
Beam width, b	2×10^{-6} m
Length of the beam, l	150×10^{-6} m
Residual stress, σ_r^a	-1.04×10^7 Pa
Stiffness of one beam, k_0	0.52 N m ⁻¹
Resistance of one beam, R_b	1130 Ω
Comb	
Finger number of a comb, n	18
Gap between the movable and stationary fingers, g	2×10^{-6} m
Poly silicon material properties ^b	
Density, ρ	2330 kg m ⁻³
Young's modulus, E^a	1.1×10^{11} Pa
Coefficient of thermal expansion, α	2.33×10^{-6} °C ⁻¹
Thermal conductivity, k_{th}	20 W m ⁻¹ °C ⁻¹

Based on:

^a Experiment of a test structure.

^b Source book data except for Young's modulus [12].

in the positive or negative region a few times. It is noted from the three modes of figure 10 that if the movable structure swings in both the regions, its vibration amplitude becomes about two times that in one-side regions.

Tunable microactuators 2 μ m in thickness have been fabricated by the standard surface micromachining process [20]. Figure 11 shows a SEM photograph of one released

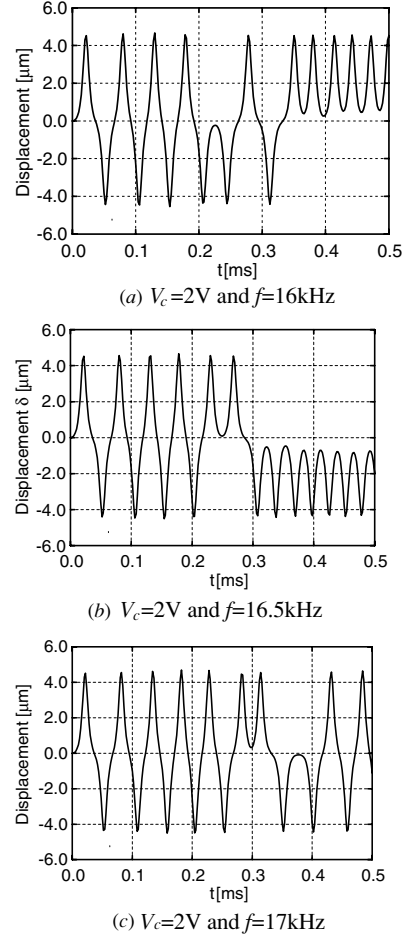


Figure 10. Simulated displacement with respect to time under the heating voltage $V_c = 2$ V and different actuating frequencies—ac driving voltage of 10 V with dc bias voltage $V_b = 40$ V. The movable structure can vibrate in three modes: (a) in the positive region, (b) in the negative region and (c) in the positive and negative regions.

Table 3. Linear and cubic stiffness coefficients of one spring beam.

k_l^a	k_{l0}	0.5172 N m ⁻¹
	k_{l1}	3.20×10^{-8} N m ⁻¹ Pa ⁻¹
k_c^b	k_{c0}	9.20×10^{10} N m ⁻³
	k_{c1}	-2.14×10^2 N m ⁻³ Pa ⁻¹
	k_{c2}	-6.17×10^{-6} N m ⁻³ Pa ⁻²

^a Calculated by using theoretical stiffness (equations (10) and (11)) and the spring beam data of table 2.

^b From curve fitting for the range of $0 \leq \delta \leq 4 \times 10^{-6}$ m and -64×10^6 Pa $\leq \sigma_i \leq 64 \times 10^6$ Pa. The data used for curve fitting are from ABACUS simulation (figure 8) with the spring beam data of table 2.

microresonator where the mass of the movable structure is 6.36×10^{-11} kg and the spring beam is 2 μ m in width and 150 μ m in length. Figure 12 is a close-up view of figure 11. The meander-shape resistor design for the purpose of electrostatic force balance has been implemented to balance the voltage supply to keep the movable structure from electrostatically sticking to the lower plate.

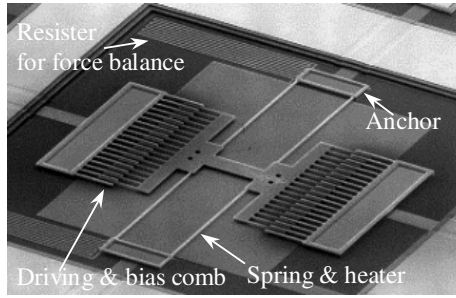


Figure 11. SEM photograph of the fabricated tunable comb drive actuator made from the standard surface-micromachining process with a total size of $360 \mu\text{m} \times 415 \mu\text{m}$.

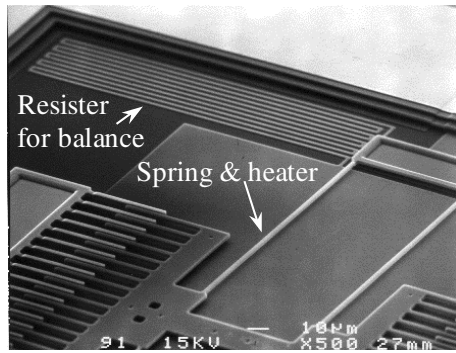


Figure 12. Close-up view of figure 11 showing combs and spring of the microactuator. A pair of meander-shape resistors is designed to balance the voltage supply to keep the movable structure from electrostatically sticking to the lower plate.

Table 4. Linear and cubic stiffness coefficients with respect to the Joule heating control voltage.

V_c (V)	σ_i^a (Pa)	k_a^b (N m^{-1})	k_b^b (N m^{-3})
0	-1.044×10^6	0.732	3.74×10^{11}
0.4	-1.19×10^7	0.551	3.75×10^{11}
0.8	-1.61×10^7	0.006 67	3.75×10^{11}
1.2	-2.32×10^7	-0.901	3.75×10^{11}
1.6	-3.31×10^7	-2.17	3.69×10^{11}
2	-4.59×10^7	-3.80	3.55×10^{11}

^a Based on initial stiffness (equations (22)) and data of table 2.

^b Calculated from equations (25) and (26). V_d of 40 V and V_a of 10 V are applied. $V_c/2$ is applied across each beam for heating.

4. Results

The tunable microactuator was tested under an optical microscope in atmospheric pressure with peak-to-peak ac driving voltage, V_a of 10 V, and dc bias voltage, V_b , ranging from 20 V to 40 V. During the experiment, the resonant frequencies, defined as the frequencies achieving maximum amplitude, are recorded. The Joule heating voltage varies in the range of 0–2 V. Figure 13 shows three sets of responses of the microactuator under different sets of applied voltages. It clearly shows that resonant frequency increases when the bias voltage V_b increases and decreases when the heating voltage V_c increases. The first set of data (circles) is response of a combination of $V_b = 40$ V and $V_c = 0$ V. The hard spring

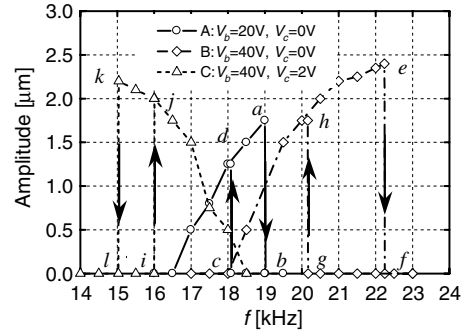


Figure 13. Experimental responses of the actuator with respect to frequency under different bias and heating voltages: bias voltage V_b increases the resonant frequency and the heating voltage V_h lowers it. The right two curves are responses for the hard spring and the left curve is a response for the apparent soft spring. a–l are points of frequency jumping for frequency sweeping.

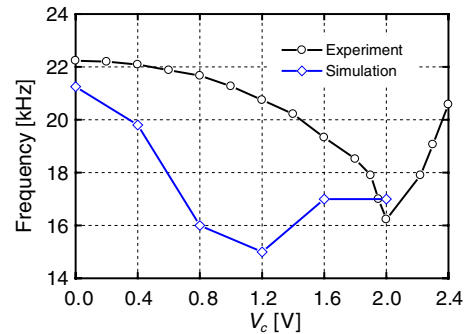


Figure 14. Measured and simulated resonant frequency from the actuator by varying heating control voltages while the bias voltage is fixed at 40 V: the experimental resonant frequency changes from 22.2 kHz to 16.2 kHz, resulting in the 27% reduction in the resonant frequency.

effect shown in equation (8) is observed due to the geometric nonlinearity of the spring beam under dc bias. The arrows from a–b and c–d indicate jump-down and jump-up phenomena, respectively. In order to examine the effect of the bias voltage on the response, the bias voltage is increased from 20 V to 40 V as shown in the second set of data (diamonds). The increase of electrostatic force results in larger resonant frequency, and higher hard spring effects due to the geometric nonlinearity of the spring. The third set of data (triangles) shows responses when the heating voltage is increased from 0 V to 2 V under the dc bias voltage of 40 V. The data show an apparent soft spring effect that is not from the negative mechanical cubic stiffness. As shown in table 4, the cubic stiffness k_b of the spring beams remains at an almost positive constant value while the Joule heating control voltage increases. The arrows of i–j and k–l are jump-up and jump-down phenomena when sweeping up down input frequencies, respectively.

Figures 14–17 summarize more experimental data. Figure 14 compares measured and simulated resonant frequency from the actuator by varying heating control voltages while the bias voltage is fixed at 40 V. The simulation result uses equation (31) and the data of tables 2 and 3. When the heating voltage increases, resonant frequency of the actuator decreases to a minimum value and increases

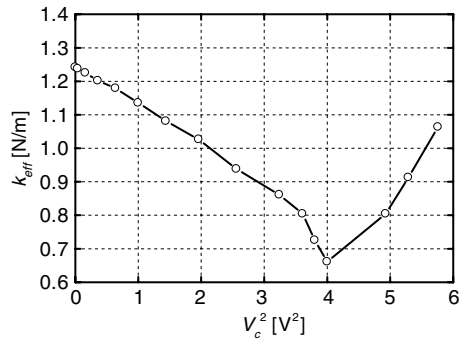


Figure 15. Effective stiffness derived from the experimental results of figure 14: stiffness is reduced by 47% from the initial stiffness of 1.24 N m⁻¹, while the heating voltage is changed from 0 V to 2 V. The stiffness increases after 2 V.

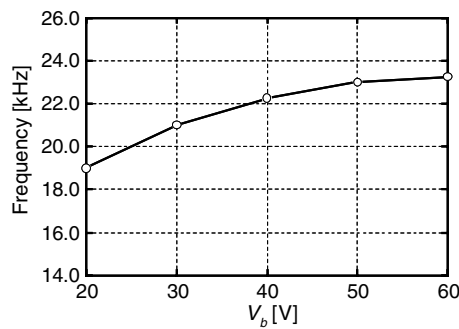


Figure 16. Resonant frequency measured from the microactuator by varying the bias voltages while the heating voltage is fixed at 0 V.

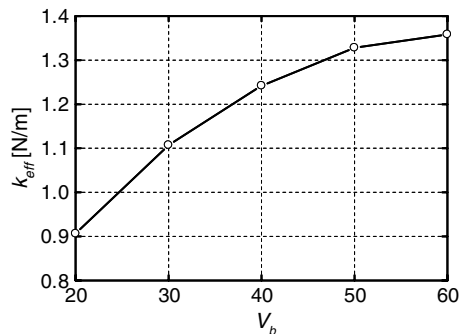


Figure 17. Effective stiffness derived from the experimental results of figure 16: stiffness is increased by 50% from the initial effective stiffness of 0.90 N m⁻¹, while the bias voltage is changed from 20 V to 60 V.

afterward. The discrepancy between the experimental and simulated frequencies might come from uncertain material properties used in the simulation. Experimentally, resonant frequency changes from 22.2 kHz to 16.2 kHz, which is 27% reduction. Figure 15 is effective stiffness data from figure 14 by using $k_{\text{eff}} = m(2\pi f)^2$. The effective stiffness is reduced by 47% from the initial stiffness of 1.24 N m⁻¹. It is noted that the effective stiffness decreases linearly with the square of heating voltage in the range of $V_c^2 = 0\text{--}3.6$ V². Figures 16 and 17 are the resonant frequency and the corresponding effective stiffness when the bias voltage V_b varies from 20 V to 40 V under $V_c = 0$ V. The resonant frequency has 24.2% increase

and the effective stiffness is increased by 50% from the initial value of 0.89 N m⁻¹. Using figures 15 and 17, a simple expression of the effective stiffness reflecting the nonlinearity on the vibration amplitude and the resonant frequency can be obtained as follows:

$$k_{\text{eff}} = 0.3488 + 3.351 \times 10^{-2} V_b - 2.787 \times 10^{-4} V_b^2 - 0.1176 V_c^2. \quad (35)$$

The above expression is an approximate equation for the effective stiffness and is valid in the range of $20 \text{ V} \leq V_b \leq 60 \text{ V}$ and $0 \leq V_c \leq 1.8 \text{ V}$.

5. Discussion

We developed a theory for the nonlinear behavior of comb drive actuators under externally induced electrostatic force and Joule heating effects. Several nonlinear sources affect the overall behavior: geometric nonlinearity of the spring, initial stress generated due to residual stress and thermally induced stress. An apparent soft spring phenomenon as well as Duffing's hard spring effect [16, 17] have been observed in figure 13. With increased bias voltage (equation (27)), the tension and stiffness of the spring increase and resonant frequency increases as shown in figure 16. The heating voltage increases to cause more Joule heating and the stiffness of the spring decreases to cause the reduction of resonant frequency as shown in figure 14. However, previous theories such as Duffing's equation did not provide good explanations on the decrease/increase of the resonant frequency in figure 14 or negative spring constant as shown in figure 13.

Figure 3 shows the spring is symmetric about the x -axis such that one may assume the spring force curve is symmetric about the origin as shown in figure 18(a). The thermal expansion of the beam gives the compressive stress and lowers the spring force and could generate negative spring constant in some regions as shown. The potential energy (stored energy) [26] corresponds to the spring force and figure 18(b) depicts the potential energy of the spring with respect to the displacement and the heating voltage. Under zero heating voltage, the curve of the potential energy is U shaped. The energy curve changes to the form of W shaped under non-zero heating voltage. As shown in figure 18(b), the curve of the W shape potential energy well is wider than that of the U shape potential energy well. The local minimum positions on a potential energy well can be defined as positions that satisfy $dE/d\delta = 0$ and $d^2E/d\delta^2 > 0$. The U shaped curve has only one stable position at $\delta = 0$ while the W shaped curve has two stable positions at either the right or left regions. At $\delta = 0$, the W shape curve is not in a stable position because the curvature is negative at the point.

Consider a mass vibrating in three different types of potential energy conditions as shown in figures 19(a), (b) and (c). E , δ , E_δ and E_b denote potential energy, displacement, maximum energy stored in the beam and barrier energy, respectively. Figure 19(a) illustrates that an actuating force such as electrostatic force may actuate the mass in the positive and negative regions. Figures 19(b) and (c) illustrate that the energy curve and barrier are adjusted by changing the heating voltages. In the case of $E_b < E_\delta$ in figure 19(b) (small heating

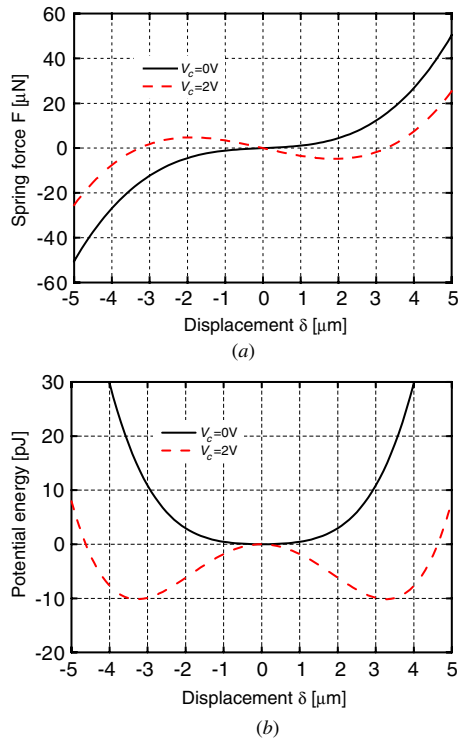


Figure 18. Spring force and corresponding potential energy while the heating control voltage V_c is changed. When V_c increases, the stiffness decreases and becomes negative in some regions. The shape of the potential energy E changes from U to W shape. The stable displacements are displacements that satisfy $dE/d\delta = 0$ and $d^2E/d\delta^2 > 0$. (a) Spring force of a beam, (b) potential energy.

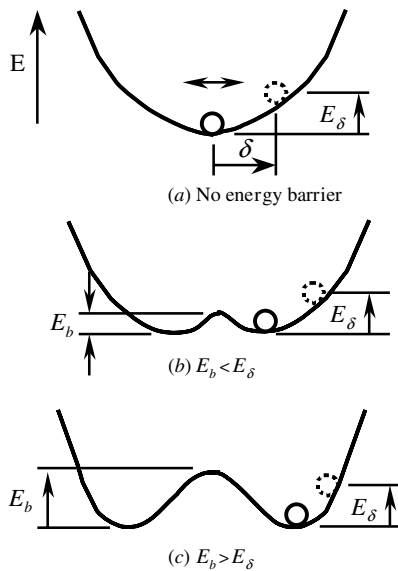


Figure 19. Explanation of the frequency shift and negative cubic stiffness: the comb drive actuator can work in the three different modes: (a) no energy barrier at the center of the energy, (b) energy barrier less than the potential energy and (c) energy barrier larger than the potential energy.

voltage), the mass could go over the energy barrier and go from one well to another. As shown in figures 18(b) and 19(b), the wider well shape provides longer vibration amplitude

and results in the lower frequency. This lower frequency phenomenon due to wider well is observed in figure 13. Moreover, the mass travels over the region of the negative linear stiffness formed in the central region of the well. This soft spring effect due to the apparent negative cubic stiffness is observed in figures 13 and 14. When we increase the heating control voltage beyond 2 V, the energy barrier is higher than the stored energy and the mass (the movable structure) cannot go over the energy barrier and its motion is confined in one well. The effect of the energy barrier on the response is observed in the numerical simulation (figure 10) at the heating control voltage of $V_c = 2$ V and at the three different frequencies of $f = 16$ kHz, 16.5 kHz and 17 kHz. From figures 10(a) and (b), the movable structure starts from $\delta = 0$, swings in the positive and negative regions a few times and then the motion of the mass is confined in the positive side well (figure 10(a), the right well figure 19(c)) or in the negative side well (figure 10(b), the left well of figure 19(c)). When the potential energy is higher than the barrier energy, the mass vibrates in the both side wells as shown in figures 10(c) and 19(b). Using this energy potential well model, we can clearly explain the frequency decrease and increase phenomenon when the heating controls voltage increases. When the heating control voltage increases until $V_c = 2$ V in figure 14, the energy well becomes wider and the potential energy well is divided into two small wells while the resonant frequency lowers. As a result, this energy well division effect of the microstructure can be used to extend travel distance of the movable structure, adjust the resonant frequency and even control the effective linear and apparent cubic stiffness over the range of negative and positive values. This energy analysis could be extended to other energy sources such as electromagnetic force for the control and operation of resonating structures.

6. Conclusions

Nonlinear behavior of the comb drive actuator under externally applied electrical actuation and Joule heating effects has been investigated analytically and experimentally. The nonlinear behavior comes from spring, electrostatic force and thermally induced stress. The linear and cubic spring constant was assumed and obtained by using a combination of theory and numerical simulation under tensile and compressive stresses. A dynamic model was built with numerical simulation to understand the nonlinear behavior of the movable structure. The dc bias voltage results in the hard spring effects. The resonant frequency decreases under Joule heating effects and the apparent negative cubic spring constant (soft spring effect) was observed. In order to explain the apparent negative cubic stiffness effect and the corresponding frequency change, we proposed the potential energy well model of the comb drive actuator where the well becomes wider and is divided into two small wells when the heating control voltage increases. From a series of experiments and numerical simulation using the developed dynamic model, the potential energy model well explained the nonlinearities of the comb drive actuator mentioned above. These investigations could lead the way to explaining nonlinearity and dynamic behaviors of complicated microsystems based on comb actuators.

References

- [1] Tang W C, Nguyen C T-C and Howe R T 1989 Laterally driven polysilicon resonant microstructures *Sensors Actuators A* **20** 25–32
- [2] Lu C, Lemkin M A and Boser B E 1995 A monolithic surface micromachined accelerometer with digital output *IEEE J. Solid-State Circuits* **30** 995–7
- [3] Geiger W, Folkmer B, Merz J, Sandmaier H and Lang W 1999 A new silicon rate gyroscope *Sensors Actuators A* **73** 45–51
- [4] Wang K and Nguyen C T-C 1999 High-order medium frequency micromechanical electronic filters *J. Microelectromech. Syst.* **8** 534–57
- [5] Welham C J, Gardner J W and Greenwood J 1996 A laterally driven micromachined resonant pressure sensor *Sensors Actuators A* **52** 86–91
- [6] Hirano T, Fan L-S, Semba T, Lee W Y, Hong J, Pattanaik S, Webb P, Juan W-H and Chan S 1999 Micro-actuator for tera-storage *Tech. Dig., IEEE Micro Electro Mechanical Systems Workshop* pp 441–6
- [7] Lee K B and Cho Y-H 1998 A triangular electrostatic comb array for micromechanical resonant frequency tuning *Sensors Actuators A* **70** 112–7
- [8] Chiao M and Lin L 2004 Post-packaging frequency tuning of microresonators by pulsed laser deposition *J. Microelectromech. Syst.* **14** 1742–8
- [9] Syms R R A 1998 Electrothermal frequency tuning of folded and coupled vibrating micromechanical resonators *J. Microelectromech. Syst.* **7** 164–71
- [10] Remtma T and Lin L 2001 Active frequency tuning for micro resonators by localized thermal stressing effects *Sensors Actuators A* **91** 326–32
- [11] Adams S G, Bertsch F M, Shaw K A and MacDonald N C 1998 Independent tuning of linear and nonlinear stiffness coefficients *J. Microelectromech. Syst.* **7** 172–80
- [12] Kovacs G T A 1998 *Micromachined Transducers: Sourcebook* (Boston: WCB/McGraw-Hill)
- [13] Kuehnel W 1995 Modeling of the mechanical behavior of a differential capacitor acceleration sensor *Sensors Actuators A* **48** 101–8
- [14] Housner G W and Hudson D E 1959 *Applied Mechanics: Dynamics* (New York: Van Nostrand)
- [15] Cho Y-H, Kwak B M, Pisano A P and Howe R T 1994 Slide film damping in laterally driven microstructures *Sensors Actuators A* **40** 31–9
- [16] Harris C M and Crede C E 1976 *Shock and Vibration Handbook* 2nd edn (New York: McGraw-Hill)
- [17] Tse F S, Morse I E and Hinkle R T 1978 *Mechanical Vibrations: Theory and Applications* 2nd edn (Boston, MA: Allyn and Bacon)
- [18] D'Souza A F and Garg V K 1984 *Advanced Dynamics: Modeling and Analysis* (Englewood Cliffs, NJ: Prentice-Hall)
- [19] ABACUS home page: <http://www.abaqus.com/>
- [20] Carter J, Cowen A, Hardy B, Mahadevan R, Stonefield M and Wilcenski S 2006 *PolyMUMPs Design Hand Book* Revision 11.0, MEMSCAP Inc., <http://www.memscap.com>
- [21] Holman J P 1981 *Heat Transfer* (New York: McGraw-Hill)
- [22] Li G and Hughes H 2000 Review of viscous damping in micro-machined structures *Micromachined Devices and Components VI, Proc. SPIE* **4176** 30–46
- [23] White F M 1974 *Viscous Fluid Flow* (New York: McGraw-Hill)
- [24] Emam S A 2002 A theoretical and experimental study of nonlinear dynamics of buckled beams *PhD Thesis* Virginia Polytechnic Institute and State University
- [25] Agarwal M, Park K K, Candler R N, Kim B, Hopcroft M A, Chandorkar S A, Jha C M, Melamud R, Kenny T W and Murmann B 2006 Nonlinear characterization of electrostatic MEMS resonators *Proc. IEEE Int. Frequency Control Symp. (Miami, FL, 4–7 June)*
- [26] Bransden B H and Joachain C J 2000 *Quantum Mechanics* 2nd edn (Harlow: Pearson Education)
- [27] Lee K B 2007 Closed-form solutions of the parallel plate problem *Sensors Actuators A* **133** 518–25